



CHALMERS
UNIVERSITY OF TECHNOLOGY

Additive Manufacturing of Interstitial Nitrogen-Strengthened CoCrNi Medium Entropy Alloy

Downloaded from: <https://research.chalmers.se>, 2024-11-19 02:20 UTC

Citation for the original published paper (version of record):

Malladi, B., Riabov, D., Guo, S. et al (2024). Additive Manufacturing of Interstitial Nitrogen-Strengthened CoCrNi Medium Entropy Alloy. *Advanced Engineering Materials*, 26(16). <http://dx.doi.org/10.1002/adem.202401182>

N.B. When citing this work, cite the original published paper.

Additive Manufacturing of Interstitial Nitrogen-Strengthened CoCrNi Medium Entropy Alloy

Sri Bala Aditya Malladi, Dmitri Riabov, Sheng Guo,* and Lars Nyborg

Equiatomic CoCrNi medium entropy alloy (MEA) is known for its excellent mechanical properties, oxidation resistance, and hydrogen embrittlement resistance. Interstitial elements like carbon and nitrogen further enhance these properties. However, there is limited research on interstitial solid solution-strengthened alloys produced via powder bed fusion-laser beam (PBF-LB). This study investigates the role of nitrogen as an interstitial alloying element in CoCrNi MEA using PBF-LB. Two alloy variants, one without nitrogen and one prealloyed with nitrogen, are analyzed through thermodynamic calculations and experimental validations. A minor nitrogen loss occurs in as-printed samples compared to prealloyed powders, but the remaining nitrogen stays as an interstitial solid solution without forming detrimental secondary phases. This leads to improved mechanical properties, with yield and ultimate tensile strengths increasing from about 690 and 900 MPa in nitrogen-free samples to over 750 and 1000 MPa in nitrogen-containing samples while maintaining the high ductility of the nitrogen-free counterpart in the as-printed materials. Additionally, the nitrogen-containing CoCrNi-N MEA exhibits $\approx 35\text{HV}$ higher hardness than the nitrogen-free variant in both as-printed and heat-treated states. These findings highlight the benefits of nitrogen addition in enhancing the mechanical properties of CoCrNi MEA produced by PBF-LB.

typically includes several remelting steps to achieve a homogeneous distribution of the elements. The production of HEAs also requires high cooling rates during solidification to avoid elemental segregation and stabilization of any detrimental phases, such as intermetallics.^[1] This makes the production process not only laborious but also difficult to fabricate components with their final geometry.

The powder bed fusion-laser beam (PBF-LB) process is an additive manufacturing (AM) process that enables the manufacturing of near-net-shape components using a high-power laser. This technology makes it possible to fabricate parts/components of nearly any geometry in a layer-by-layer manner.^[2–4] Owing to rapid melting and solidification, atomic diffusion and hence elemental segregation are limited, which reduces the possibility of forming detrimental phases in the produced parts.^[5–7]

Equiatomic CoCrNi is one of the most widely researched MEAs owing to its excellent strength and ductility at room


temperature, oxidation and corrosion resistance, hydrogen embrittlement resistance, and cryogenic mechanical properties.^[8–15] The addition of interstitial elements such as carbon and nitrogen is known to further improve the properties of HEAs (known as interstitial HEAs, or iHEAs) by interstitial solid solution strengthening and lowering the stacking fault energy, hence provoking the twinning-induced plasticity effect.^[16–24] Although interest in the AM of HEAs is rapidly increasing, there has been little focus on the development of iHEAs for AM.

The aim of this study is to explore the effect of nitrogen as an interstitial element in a CoCrNi MEA produced using PBF-LB. The influence of nitrogen addition on the microstructure and room-temperature mechanical properties of the alloy was evaluated. Two variants of the equiatomic CoCrNi MEA, one without nitrogen and the other prealloyed with 0.18 wt% of nitrogen, were studied. It was observed from both thermodynamic calculations and experimental studies that nitrogen is stable as an interstitial element in the as-printed material, devoid of any detrimental phase during the printing process. It was also found that the addition of nitrogen mildly improved the hardness, yield strength (YS), and ultimate tensile strength (UTS) while maintaining the ductility of the nitrogen-free counterpart in the as-printed materials.

1. Introduction

High entropy alloys (HEAs) are a new class of alloys consisting of five or more elements in nearly equiatomic ratios, with a high entropy of mixing (ΔS_{mix} , intended to stabilize the formation of the solid solution phase). Based on the values of ΔS_{mix} , the alloys can be further classified as HEAs ($\Delta S_{\text{mix}} > 1.5R$), medium entropy alloys (MEAs) ($1.0R \leq \Delta S_{\text{mix}} \leq 1.5R$), and low entropy alloys ($\Delta S_{\text{mix}} \leq 1.0R$), where R is the gas constant. The commonly used way to produce HEAs and MEAs is casting, which

S. B. A. Malladi, D. Riabov, S. Guo, L. Nyborg
Department of Industrial and Materials Science
Chalmers University of Technology
Gothenburg SE-41296, Sweden
E-mail: sheng.guo@chalmers.se

 The ORCID identification number(s) for the author(s) of this article can be found under <https://doi.org/10.1002/adem.202401182>.

© 2024 The Author(s). Advanced Engineering Materials published by Wiley-VCH GmbH. This is an open access article under the terms of the Creative Commons Attribution License, which permits use, distribution and reproduction in any medium, provided the original work is properly cited.

DOI: 10.1002/adem.202401182

2. Experimental Section

Two different grades of gas-atomized powder based on an equiatomic CoCrNi MEA, one without and the other prealloyed with nitrogen, were supplied by Höganäs AB. Both variants of the powder had a spherical morphology and were provided with a particle size range of 15–45 μm . Bulk chemical analysis of the powder and printed samples was performed using induction-coupled plasma optical emission spectrometry (ICP-OES). The nitrogen and oxygen concentrations of the powder and printed samples were measured using a LECO CS-844 combustion analyzer. The chemical compositions of the powder variants and printed samples are summarized in **Table 1**. Compared to the prealloyed gas-atomized powder, a slight loss of nitrogen was observed in the as-printed samples.

The parts were built in an EOS M100 PBF-LB machine equipped with 200 W Yb-fiber laser and a spot diameter of 40 μm . The build chamber was purged with argon gas prior to printing to maintain an oxygen level of 1000 ppm. Two-factor D-optimal design of experiments (DOE) was implemented using the JMP software (version 16.0; SAS Institute, Cary, NC, USA) to evaluate the influence of printing parameters on the densification of both CoCrNi and CoCrNi-N alloys. The hatch distance was varied between 0.06 and 0.1 mm, and the scan speed was varied between 400 and 1200 mm s^{-1} . The laser power and layer thickness were maintained constant at 110 W and 20 μm , respectively, for the DOE. Cubes with dimensions of 10 \times 10 \times 10 mm were built with the parameters obtained from the DOE. The schematic of the cube showing a 67° scan rotation with respect to the orientations of the sample, and the design space for the two-factor DOE, are shown in **Figure 1**.

The printed samples were first subjected to sequential grinding using SiC emery papers of 220–1000 grit, followed by

sequential polishing using suspended diamond solutions with diamond sizes of 9, 3, and 1 μm . Final polishing was performed using a colloidal solution consisting of 40 nm sized SiO₂ particles. Optical microscopy images of the entire cross-section of the polished samples were taken using a Zeiss Axiovision 7 microscope equipped with a Zeiss digital camera 35 and Axio Vision software. The acquired images were processed using Fiji ImageJ software for density/porosity analysis using the contrast threshold method.^[25] Both alloys were etched using an aqua regia solution (3:1 volume mixture of HCl and HNO₃) to reveal the solidification structure.

Scanning electron microscopy (SEM) and electron backscattered diffraction (EBSD) were performed using the LEO Gemini 1550 SEM equipped with a Nordlys II detector (Oxford Instruments). EBSD analysis was performed at an acceleration voltage of 20 kV and a step size of 0.15 μm . The obtained EBSD raw data were analyzed using MTEX, an open-source MATLAB toolbox.^[26] X-Ray diffraction (XRD) was performed to identify the phases present in the powder and bulk samples using a Bruker AXS D8 Advance diffractometer equipped with a Cr K α source ($\lambda = 2.28970 \text{ \AA}$) operated at 35 kV and 40 mA.

The Vickers hardness of both alloys was measured using a Struers Durascan 70G5 (Ballerup, Denmark) instrument with a load of 1 kg and a duration of 15 s. Samples of 55 \times 10 \times 10 mm were printed in the horizontal orientation and tensile bars with a gauge length of 12.5 mm, width of 2.5 mm, and thickness of 1 mm were machined using electric discharge machining (EDM). The surfaces of the machined samples were subjected to grinding with SiC emery sheets, starting from 800 grits and all the way down to 2000 grits, to avoid the influence of the EDM process. Tensile tests were performed using a SHIMADZU, AG-100kN Xplus tester at a strain rate of $1 \times 10^{-3} \text{ s}^{-1}$. The strain analysis was performed using digital image correlation (Vic-2D, Correlated Solutions).

Table 1. Chemical compositions of powder and as-printed samples.

Material	Co [wt%]	Cr [wt%]	Ni [wt%]	N [wt%]	O [wt%]
CoCrNi (Powder)	34.05	29.80	36.10	0.003	0.038
CoCrNi-N (Powder)	34.4	30.70	34.60	0.18	0.04
CoCrNi (As-printed)	34.05	29.80	36.10	0.002	0.038
CoCrNi-N (As-printed)	34.48	30.76	34.6	0.12	0.04

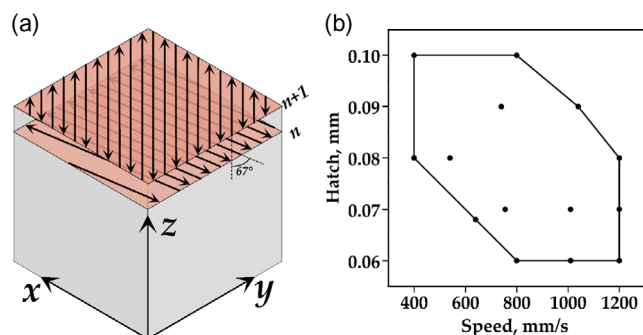


Figure 1. a) Schematic showing 67° scan rotation between successive layers and b) two-factor D-optimal design space showing the variations in scan speed and hatch distance.

3. Thermodynamic Calculations

Phase equilibria and phase transformations were depicted using Thermo-Calc,^[27] following the CALPHAD (CALculation of PHase Diagram) method and using the TCHEA4 database, with the composition of CoCrNi-N (0.12 wt% N) measured from the as-printed sample (Table 1). The predicted equilibrium phase fractions versus temperature for the CoCrNi-N system are shown in **Figure 2**. As can be seen, solidification to the face centered cubic (fcc) phase is expected to start at 1430 °C, while some detrimental phases such as the sigma, pi, and nitrogen-rich Cr₂N phases (indicated as the hcp phase in Figure 2) are predicted to form at equilibrium conditions below the melting point. However, as the kinetic constraints imposed owing to the fast-cooling rates in PBF-LB, it is expected that the formation of the indicated phases is suppressed, whereby nitrogen is stabilized as an interstitial element and the formation of detrimental phases in the as-printed samples is avoided.

From the phase equilibria plot in Figure 2, it could be expected that nitrogen would react with chromium given sufficient time between 800 and 1200 °C, resulting in the precipitation of Cr₂N. To experimentally verify the stability of nitrogen as an interstitial element in the as-printed materials and to explore the possible

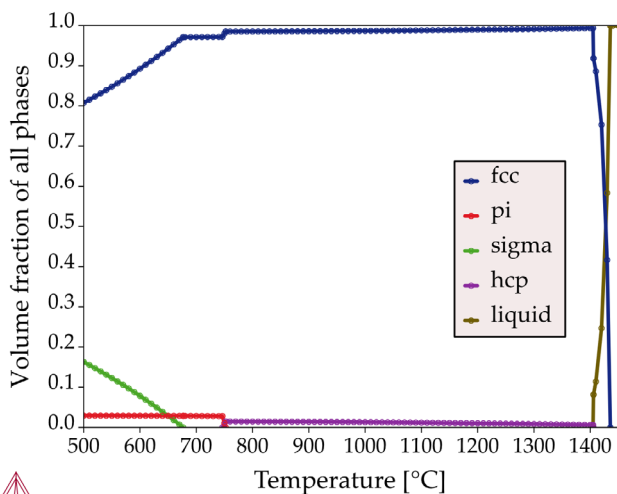


Figure 2. Equilibrium phase fractions of all phases in the CoCrNi-N (0.12 wt% N) system calculated using Thermo-Calc.

post-PBF-LB formation of Cr_2N , heat-treatment experiments were designed based on calculations using TC-Prisma. The resulting continuous cooling transformation (CCT) curves are drawn at cooling rates ranging from 0.01 to 100 K s^{-1} from $1500 \text{ }^\circ\text{C}$, and the time required for the start of the formation of Cr_2N at each of the cooling rates is overlapped on those curves, as shown in **Figure 3a**, while **Figure 3b** shows the predicted time-temperature-transformation (TTT) diagram for the same starting condition. From **Figure 3a**, the precipitation of Cr_2N occurs mainly inside the bulk and no precipitation was predicted at the grain boundaries. It was also predicted that the formation temperatures for Cr_2N are seen to be lower at faster cooling rates. Based on these calculations, isothermal heat treatments were performed for the as-printed samples of both CoCrNi and CoCrNi-N for 30 min (1800 s) each at 800, 900, 1000, 1100, and $1200 \text{ }^\circ\text{C}$, i.e., the critical temperature range for the formation of Cr_2N , as shown in **Figure 3b**.

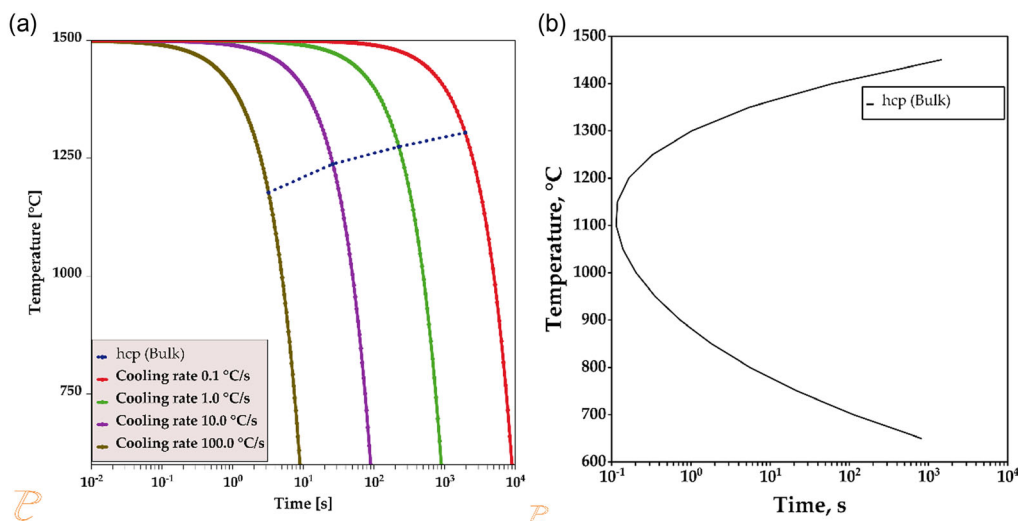


Figure 3. a) TC-Prisma calculations to predict the nucleation kinetics of the formation of Cr_2N using CCT and b) TTT diagrams.

4. Experimental Results and Discussion

4.1. DOE and Relative Density of Printed Samples

The contour plots obtained from the DOE analysis based on the assessment of the relative density by quantitative optical microscopy on the cross-sections of CoCrNi and CoCrNi-N are shown in **Figure 4**. More than 50% of the combination of processing parameters from DOE resulted in a density greater than 99.5% for both materials, suggesting good overall printability. The processing of CoCrNi-N appeared to be even more robust than that of CoCrNi, with a higher number of parameters yielding a density greater than 99.5%. ICP-OES on the printed samples revealed loss of nitrogen during the printing process, as mentioned in **Table 1**. This nitrogen loss is due to the limited solubility of nitrogen in the liquid phase as compared with the solid phase.^[28,29] Notably, with nitrogen being the sole distinction between the two alloys, prealloying nitrogen in the powder appears to enhance the densification behavior during the printing process. The significance of the fitted model is usually measured using the determination coefficient (RSq) and the p -value. The models for both alloys showed RSq values greater than 99.8% and p -values of less than 0.001. A higher RSq value signifies that the model predicts the variation in parameters with greater than 99.8% confidence, and it was predicted that the speed influences the densification more than the hatch distance. An exceedingly small p -value indicated that the model's prediction was statistically significant. Based on the results obtained from the DOE, the highest measured density ($\approx 99.9\%$) was observed at a scan speed of 1010 mm s^{-1} and hatch distance of 0.07 mm , at a fixed laser power of 110 W and layer thickness of 0.02 mm . The parts were produced using these printing parameters for further characterization and analysis.

4.2. XRD

Figure 5 shows the XRD patterns of the as-received powder and the as-printed samples of the CoCrNi and CoCrNi-N alloys.

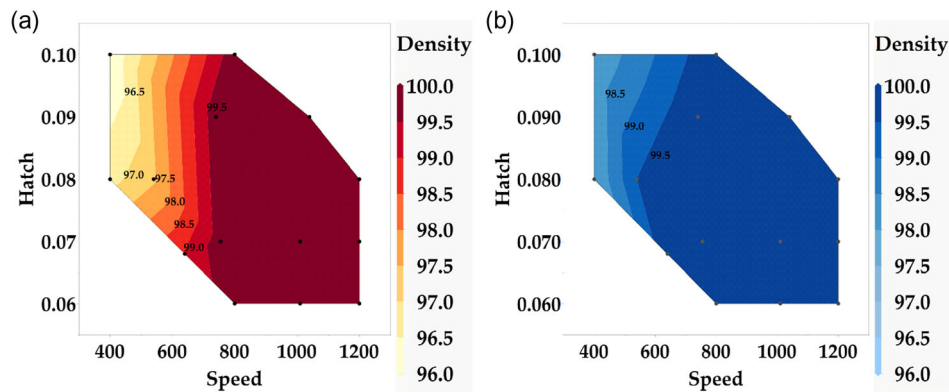


Figure 4. a) Contour plots showing the densification regions in terms of relative density based on the two-factor D-optimal DOE for CoCrNi and b) CoCrNi-N MEAs.

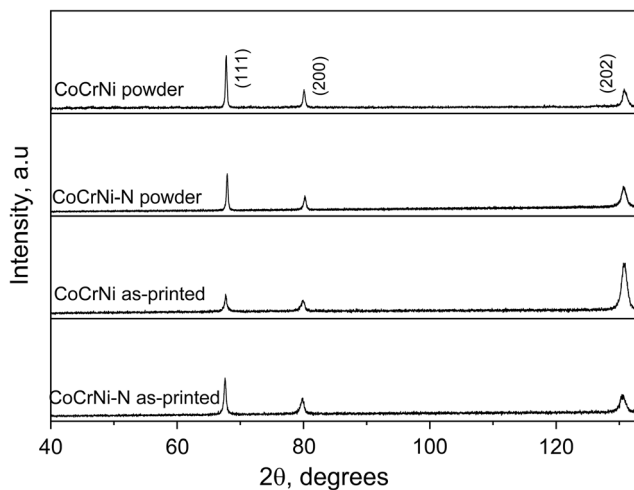


Figure 5. XRD patterns of gas-atomized powder and as-printed samples of CoCrNi and CoCrNi-N.

From the diffraction patterns, all samples exhibit a single fcc phase. This means that either none of the detrimental phases predicted to exist under equilibrium conditions are present in the powder samples and the as-printed samples, or their volume fractions are too low to be detected by XRD.

4.3. Microstructural Characterization

4.3.1. As-Printed Samples

A typical mixture of elongated and equiaxed cellular solidification structures for the CoCrNi MEA is shown in **Figure 6a**. A similar solidification structure was observed for the CoCrNi-N. Both materials also show epitaxially grown columnar grains in the x - z orientation, spanning across several melt pools. The seen epitaxial growth of columnar grains and cellular solidification structures is typical morphological characteristics of the microstructure generated in the PBF-LB process because of the high local thermal gradients during solidification.^[30–33] It has also been previously reported that cell size correlates with the local thermal gradient

and local growth rate in the melt, and cell size decreases with increasing thermal gradients and growth rate, which represents the local cooling rate.^[34–36] The difference in the size and orientation of the cells observed in the two materials in the x - z orientation is supposed to be due to the different thermal gradients and solidification velocities within one melt pool.

Scheil solidification simulations were performed to predict the elemental redistribution during the solidification pathway of the CoCrNi and CoCrNi-N MEAs to understand which elements tend to accumulate in intercellular locations^[31] and the results are shown in **Figure 7**. It can then be seen that among the principal elements, Cr is supposed to segregate to the cell walls for both materials (**Figure 7a,b**). In addition, for CoCrNi-N, along with chromium, nitrogen was predicted to accumulate in the cell walls (**Figure 7c**).

4.4. EBSD

Figure 8 shows the EBSD orientation maps of CoCrNi and CoCrNi-N in the x - z orientation. As evident from the inverse pole figures in **Figure 8c,d**, CoCrNi shows a $\langle 110 \rangle$ texture, whereas CoCrNi-N shows a mixture of $\langle 001 \rangle$ and $\langle 110 \rangle$ textures in the x - z orientation. However, since both alloys in the present study were printed using the same printing parameters, the difference in the texture observed is caused mainly due to the addition of nitrogen. Although fcc materials fabricated with PBF-LB are supposed to show a $\langle 001 \rangle$ texture along the building direction, Sun et al. reported that it is possible to engineer the $\langle 011 \rangle$ texture in 316 L by manipulating the printing parameters.^[37] Pham et al. reported that in PBF-LB, the scan rotation influences the solidification behavior (thermal gradients and velocity of solidification front), resulting in the $\langle 001 \rangle$ orientation of grains being parallel to the build direction. Furthermore, they also demonstrated that cells could change the direction by side-branching along perpendicular $\langle 001 \rangle$ directions, resulting in complex growth paths.^[38] It was also reported that materials with a $\langle 011 \rangle$ texture could enhance the formation of nanotwinning, resulting in improved YS, ductility, and toughness of the parts.^[37,39] Hence, in the current scenario, a 67° rotational scan was employed during the printing process. This strategy aimed to

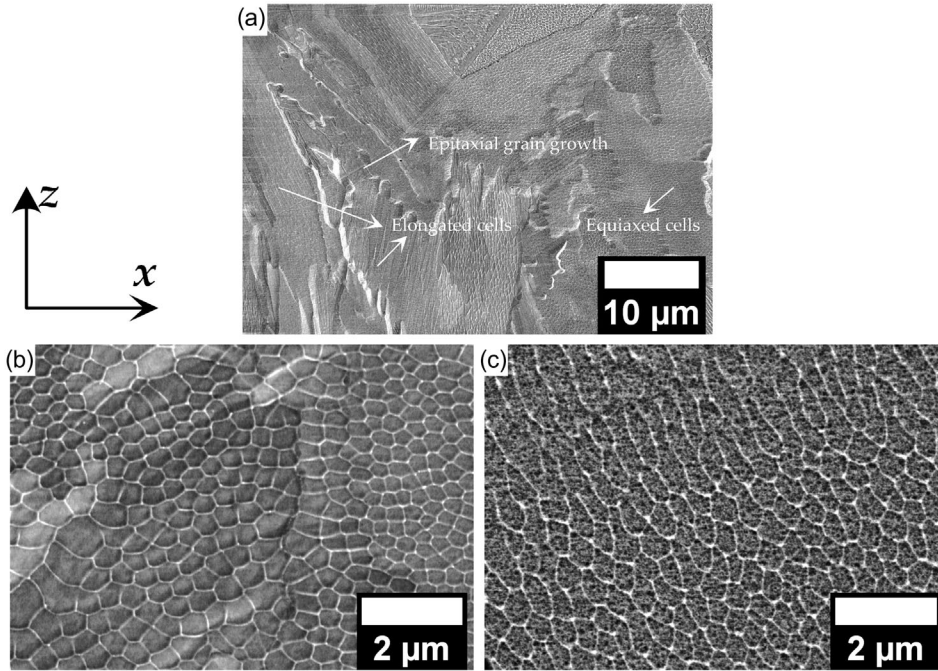


Figure 6. a) SEM images showing the epitaxially grown columnar grains and their internal cellular solidification structure in the as-printed samples at lower magnification for CoCrNi, and at higher magnifications for b) CoCrNi and c) CoCrNi-N in the x-z orientation.

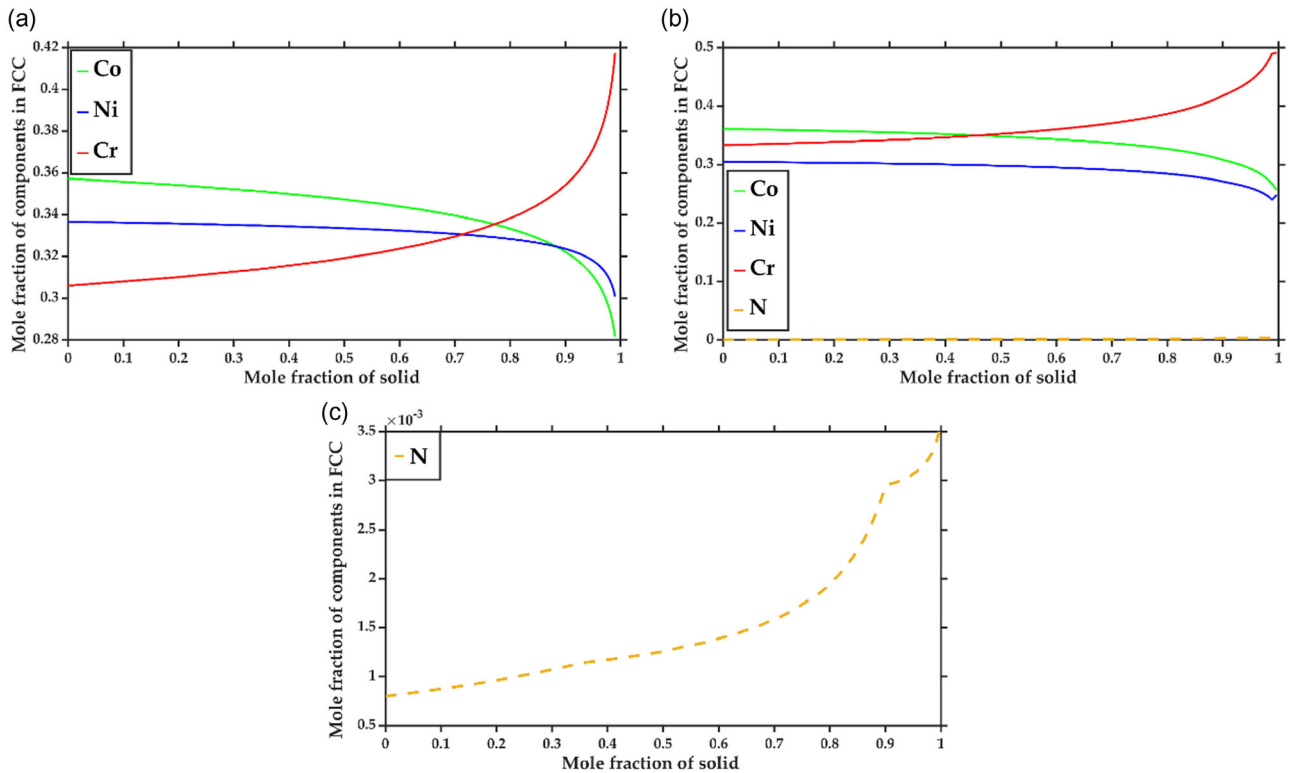


Figure 7. a) Scheil solidification curves showing elemental segregation in CoCrNi, b) CoCrNi-N, and c) magnified curve showing segregation of nitrogen in CoCrNi-N.

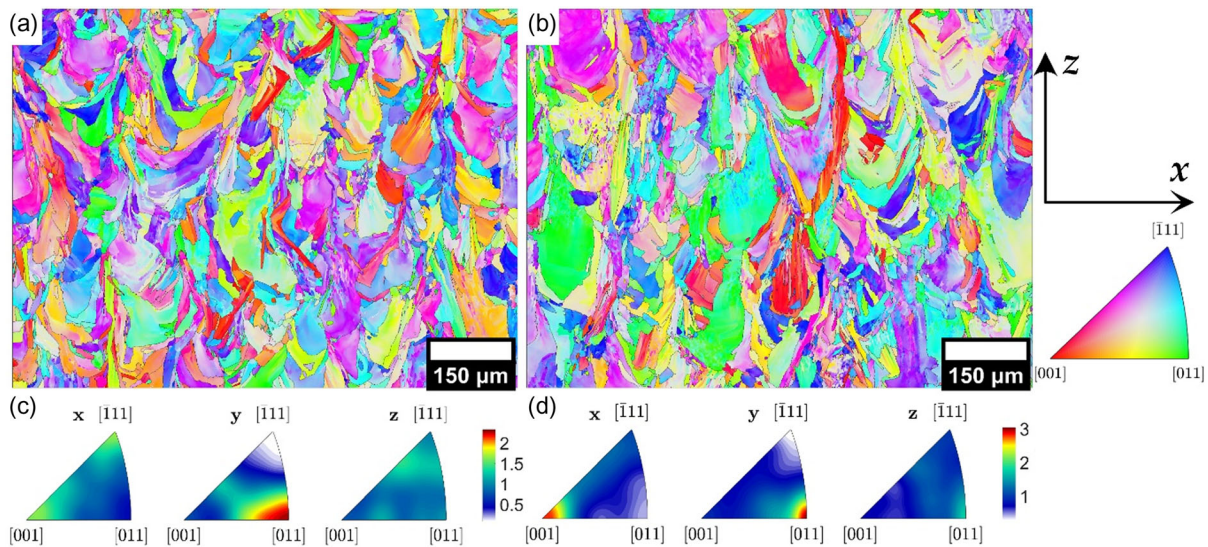


Figure 8. a,c) EBSD orientation maps and their respective inverse pole figures of the as-printed samples of CoCrNi and b,d) CoCrNi-N in the x-z orientation.

mitigate epitaxial grain growth by interrupting thermal gradients and growth rates, ultimately minimizing microstructural anisotropy and consequently, mitigating mechanical anisotropy.

In terms of the grain size, it was found from EBSD analysis that the average grain sizes of 7.4 μm and 6.6 μm were obtained for CoCrNi and CoCrNi-N, respectively. These grain sizes in as-printed samples are substantially smaller compared to what has been observed for cast CoCrNi ($\approx 45 \mu\text{m}$) as well as for as-printed CoCrNi ($\approx 25 \mu\text{m}$). It has been previously reported that grain size can be influenced by manipulating the PBF-LB printing parameters.^[33,40,41] The smaller grain size in the as-printed samples in the present study could help obtain better mechanical performance of both materials compared to that of the coarser-grained material.

4.5. Microstructural Characterization of Heat-Treated Samples

From phase identification and microstructural observations, it is clear that nitrogen did not lead to the formation of any detrimental phase and is stable as an interstitial element. **Figure 9** and **10** show the backscattered electron mode of SEM micrographs of the as-printed and heat-treated samples of CoCrNi and CoCrNi-N, respectively. The microstructure was not significantly affected by the heat treatment up to 1100 $^{\circ}\text{C}$. However, in both materials, heat treatment at 1200 $^{\circ}\text{C}$ led to a recrystallized microstructure (Figure 9f and 10f). The presence of small spherical particles was observed in both samples after heat treatment, which seemed to decorate what looks like the cell boundaries after heat treatment at 800 $^{\circ}\text{C}$ (Figure 9b and 10b). As the heat treatment

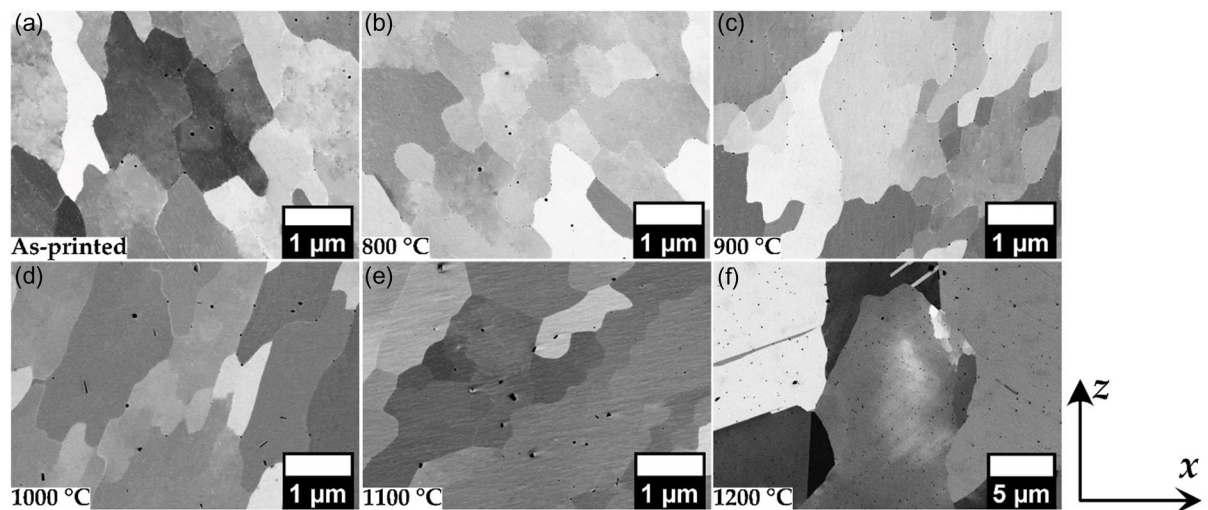


Figure 9. Backscattered SEM images in the building direction of heat-treated CoCrNi samples. a) as-printed; b–f): after heat treatment at 800 $^{\circ}\text{C}$, 900 $^{\circ}\text{C}$, 1000 $^{\circ}\text{C}$, 1100 $^{\circ}\text{C}$, and 1200 $^{\circ}\text{C}$, respectively.

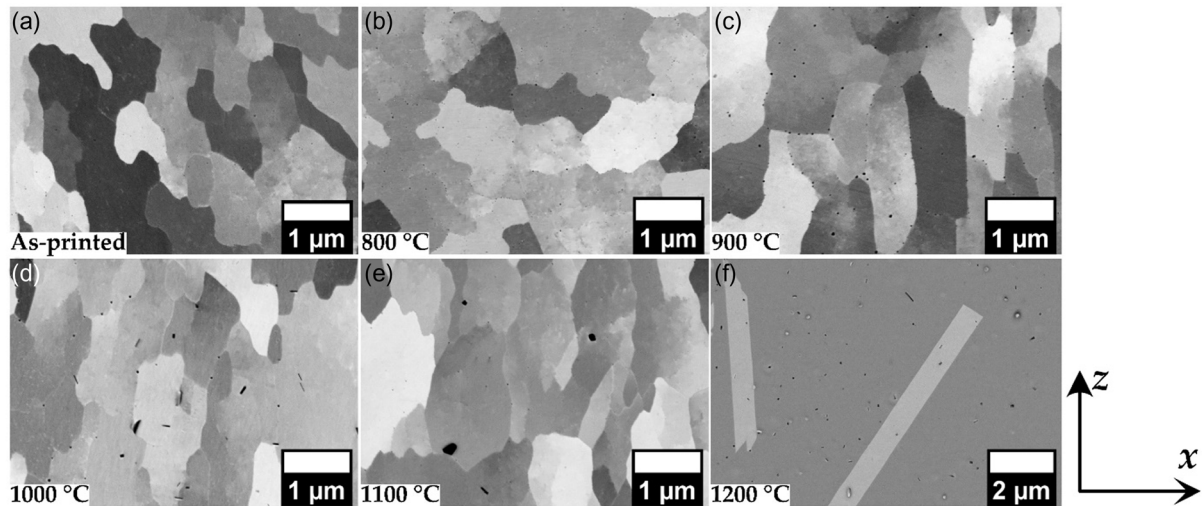


Figure 10. Backscattered SEM images in the building direction of heat-treated CoCrNi-N in x-z orientation. a) as-printed; b–f): after heat treatment at 800 °C, 900 °C, 1000 °C, 1100 °C, and 1200 °C, respectively.

temperature increased to 900 °C, both the size and number density of the particles seemed to increase. Further increasing the temperature led to the particles predominantly increasing in size, resulting in an average size of ≈ 200 nm following heat treatments at 1200 °C. Specifically, three different types of particles were identified: 1) dark particles with a cuboidal morphology, 2) dark rod-shaped particles, and 3) bright particles. Surprisingly, energy dispersive spectroscopy (EDS) line scans of all three types of particles observed in the CoCrNi-N sample after heat treatment at 1200 °C revealed that they are chromium-rich oxides, as shown in **Figure 11**, and no indication of Cr_2N precipitation was observed.

4.6. Hardness

Hardness tests were performed to understand the influence of nitrogen on the mechanical behavior of CoCrNi and CoCrNi-N MEAs in both as-printed and heat-treated conditions.

The results are shown in **Figure 12**. In the as-printed state, CoCrNi-N exhibited ≈ 35 HV higher hardness compared with that of CoCrNi. The samples heat-treated at 800 °C and 900 °C showed similar hardness values to the as-printed samples. With a further increase in the heat-treatment temperature, both materials started to soften, while the difference in hardness between both materials remained almost constant, ≈ 35 HV. The samples heat-treated at 1200 °C showed recrystallized microstructures (Figure 9f and 10f), which also resulted in a large decrease in hardness to 200 and 238 HV, respectively, much lower compared with the as-printed hardness values for CoCrNi (278 HV) and CoCrNi-N (320 HV).

4.7. Tensile Properties

Figure 13 shows the room-temperature engineering stress–strain curves for the as-printed CoCrNi and CoCrNi-N MEAs. The YS

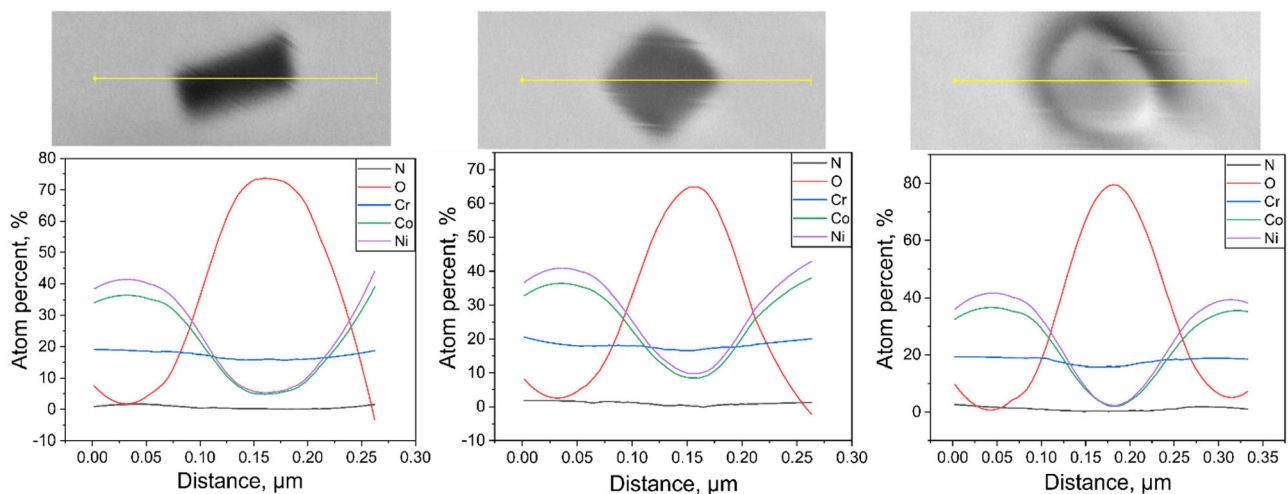


Figure 11. EDS analysis of the particles observed in CoCrNi-N heat-treated at 1200 °C.

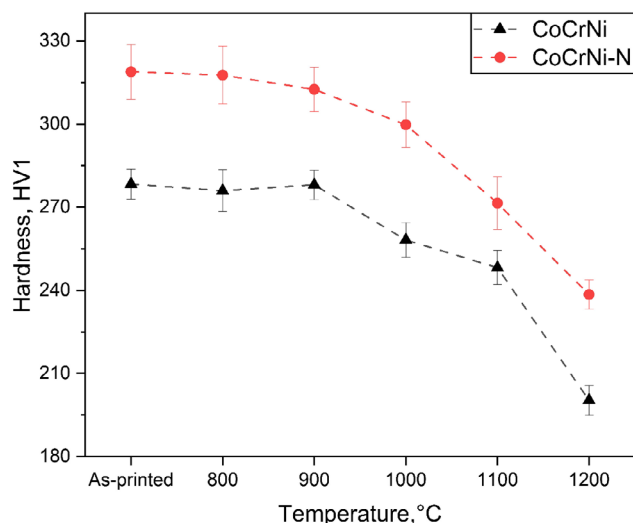


Figure 12. Hardness plot of as-printed and heat-treated samples showing the influence of heat treatments on CoCrNi and CoCrNi-N MEAs.

and UTS values obtained from the tensile tests are shown in **Table 2**. These results agree with the hardness results and show that alloying with nitrogen has a clear positive effect on the tensile properties. Even so, the tensile properties (YS, UTS, and ductility) of the nitrogen-free CoCrNi were significantly improved compared to those previously reported for CoCrNi, either prepared by casting or PBF-LB,^[24,42] which could be primarily due to the significantly smaller grain size that was achieved in

this study. A slight difference in the ductility was observed between these two alloys, with CoCrNi showing relatively high ductility when tested in both XY and XZ orientations as compared to the CoCrNi-N variant. The variation in mechanical properties across different building directions is due to the anisotropy present in both the microstructure and texture of the as-printed parts, as discussed in Section 4.4, which is a characteristic of the PBF-LB process.^[43–45] This anisotropy could be minimized to an extent by manipulating the scan strategy during the printing process, which influences the thermal gradients and the cooling rates.

Examining the stress–strain curves for CoCrNi and CoCrNi-N, the main distinction is the higher YS and UTS for the latter material. When the plastic stress–strain regimes of both materials are overlaid, their work-hardening responses are essentially identical, which is also evidenced by the similar level of work hardening (UTS–YS, as shown in Table 2). Therefore, the primary effect of nitrogen as an interstitial element is linked to effective solid solution strengthening, even at low nitrogen concentrations. The elastic modulus (E) calculated from the elastic regions for both alloys with respect to different printing directions are presented in Table 2. In case of CoCrNi, the value of E is lower for the XZ orientation as compared to XY, indicating the influence of the texture in the as-printed state. However, in case of CoCrNi-N, the difference in E between XZ and XY planes is significantly less (≈ 50 MPa). The decrease in elastic anisotropy with the addition of nitrogen can likely be attributed to the combined effect of enhanced austenitic cell stability and the strong bonding of nitrogen with the surrounding solute atoms.^[46]

Comparing the properties of both CoCrNi and CoCrNi-N produced by PBF-LB in the present study with the same alloys

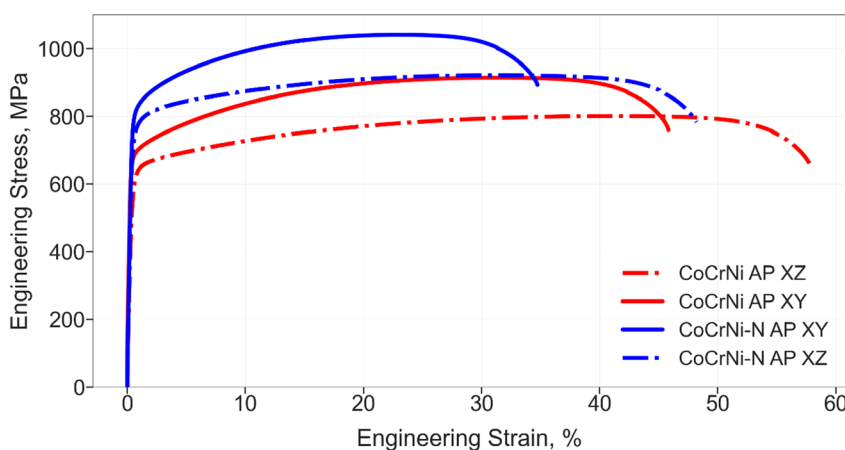


Figure 13. Engineering stress–strain curves of as-printed samples of CoCrNi and CoCrNi-N.

Table 2. YS and UTS values measured from as-printed samples of both CoCrNi and CoCrNi-N in XY and XZ directions.

Alloy	Orientation	YS [MPa]	UTS [MPa]	Elongation to fracture [ϵ_f , %]	UTS–YS [MPa]	Elastic modulus [MPa]
CoCrNi	XZ	584.2 \pm 8.6	809.1 \pm 5.4	53.7 \pm 4.5	\approx 225	1431
	XY	690.7 \pm 32.9	915.3 \pm 1.0	42.5 \pm 2.1	\approx 225	1823
CoCrNi-N	XZ	723.5 \pm 21.7	927.24 \pm 5.2	49.1 \pm 1.3	\approx 204	1727
	XY	785.2 \pm 62	1044.9 \pm 3.5	36.6 \pm 2.8	\approx 259	1777

containing similar levels of nitrogen but manufactured using the thermomechanical processing route, the YS of the alloys in the present study is much higher. This, however, comes at the expense of reduced ductility. For example, in the work performed by Moravcik et al.^[19] both CoCrNi and CoCrNi-N (0.117 wt% N) were prepared using the thermomechanical processing route, and these alloys showed YS of 282 and 565 MPa and UTS of 836 and 1069 MPa for CoCrNi with grain sizes of 45 and 2.6 μm , respectively, and YS of 375 and 703 MPa and UTS of 899 and 1052 MPa for CoCrNi-N (0.117 wt% N) with grain sizes of 43 μm and 2.6 μm , respectively. The comparison shows that the PBF-LB processing has significant improvement in YS of the alloys, which could mainly be due to the relatively high dislocation densities in the alloys due to the successive thermal cycling, which is inherent to the PBF-LB processing technique.^[47–49]

It has been previously reported that CoCrNi has an intrinsically low stacking fault energy, which results in the easy formation of nanotwins upon deformation, particularly at cryogenic temperatures.^[8,9,50] The addition of interstitial nitrogen is also known to improve the ductility and strength of MEAs,^[18,19,21] which could account for the improved mechanical properties of CoCrNi-N compared to those of CoCrNi. However, such an effect tends to yield a different work-hardening response, which is not observed in the current case. Consequently, the results indicate that the major effect is the pure solid solution strengthening effect of the single-phase structure by interstitial nitrogen.

5. Conclusion

The microstructures of the as-printed samples of both CoCrNi and CoCrNi-N MEAs showed a cellular solidification structure. Scheil solidification simulations suggested elemental segregation of chromium and nitrogen in the cell walls during solidification. CoCrNi showed a $\langle 011 \rangle$ texture in the build direction with an average grain size of 7.4 μm , while a mixture of $\langle 001 \rangle$ and $\langle 011 \rangle$ textures was observed for the CoCrNi-N MEA with an average grain size of 6.6 μm . The samples heat treated at 800 °C and above were devoid of Cr₂N precipitates; instead, the formation of chromium-rich oxides across the cell boundaries was observed after heat treatment. The particle sizes grew with increasing heat treatment temperature, suggesting an internal coarsening mechanism for oxide particles in the materials. Both materials experienced recrystallization when subjected to heat treatment at 1200 °C. The CoCrNi-N MEA consistently displayed an $\approx 35\text{HV}$ higher hardness compared to CoCrNi, in both as-printed and heat-treated samples, highlighting a distinct solid solution strengthening effect induced by nitrogen. Variations in the mechanical properties with respect to the building orientations were observed, which are mainly due to microstructural anisotropy. It is worth noting that both materials exhibited significant ductility, underscoring their inherent toughness, a characteristic hallmark of these alloys.

Acknowledgements

This study was conducted as part of the Competence Center for Additive Manufacturing—Metals (CAM2) (2016-05175) with support from the

Swedish Innovation Agency (VINNOVA) and the Production Area of Advance. Technical cooperation with Höganäs AB and the cooperation and contributions from Adjunct Professors Karin Frisk and Sven Bengtsson are gratefully acknowledged.

Conflict of Interest

The authors declare no conflict of interest.

Author Contributions

Sri Bala Aditya Malladi: Conceptualization (supporting); Data curation (lead); Formal analysis (lead); Investigation (lead); Methodology (lead); Validation (lead); Writing—original draft (lead). **Dmitri Riabov:** Investigation (supporting); Methodology (supporting); Writing—review and editing (supporting). **Sheng Guo:** Conceptualization (lead); Formal analysis (supporting); Project administration (lead); Resources (supporting); Supervision (lead); Writing—review and editing (lead). **Lars Nyberg:** Conceptualization (supporting); Funding acquisition (lead); Supervision (supporting); Writing—review and editing (supporting).

Data Availability Statement

The data that support the findings of this study are available from the corresponding author upon reasonable request.

Keywords

interstitial solid solution strengthening, laser powder bed fusion, mechanical properties, medium entropy alloys, microstructural characterization

Received: May 17, 2024

Revised: July 11, 2024

Published online: August 3, 2024

- [1] S. Guo, *Mater. Sci. Technol.* **2015**, *31*, 1223.
- [2] W. E. Frazier, *J. Mater. Eng. Perform.* **2014**, *23*, 1917.
- [3] D. Herzog, V. Seyda, E. Wycisk, C. Emmelmann, *Acta Mater.* **2016**, *117*, 371.
- [4] D. J. Horst, R. D. A. Vieira, *Int. J. Eng. Tech. Res.* **2018**, *8*, 3.
- [5] Y. Brif, M. Thomas, I. Todd, *Scr. Mater.* **2015**, *99*, 93.
- [6] S. Chen, Y. Tong, P. K. Liaw, *Entropy* **2018**, *20*, 937.
- [7] D. Karlsson, A. Marshal, F. Johansson, M. Schuisky, M. Sahlberg, J. M. Schneider, U. Jansson, *J. Alloys Compd.* **2019**, *784*, 195.
- [8] H. Huang, J. Wang, H. Yang, S. Ji, H. Yu, Z. Liu, *Scr. Mater.* **2020**, *188*, 216.
- [9] J. P. Liu, J. X. Chen, T. W. Liu, C. Li, Y. Chen, L. H. Dai, *Scr. Mater.* **2020**, *181*, 19.
- [10] C. K. Soundararajan, H. Luo, D. Raabe, Z. Li, *Corros. Sci.* **2020**, *167*, 108510.
- [11] F. Weng, Y. Chew, Z. Zhu, S. Sui, C. Tan, X. Yao, F. L. Ng, W. K. Ong, G. Bi, *Compos. B Eng.* **2021**, *216*, 108837.
- [12] B. Gludovatz, A. Hohenwarter, K. V. S. Thurston, H. Bei, Z. Wu, E. P. George, R. O. Ritchie, *Nat. Commun.* **2016**, *7*, 10602.
- [13] J. Wang, W. Li, H. Yang, H. Huang, S. Ji, J. Ruan, Z. Liu, *Corros. Sci.* **2020**, *177*, 108973.
- [14] J. Wang, J. Zou, H. Yang, Z. Liu, S. Ji, *Mater. Sci. Eng. A* **2022**, *843*, 143129.

- [15] J. Wang, H. Yang, Z. Liu, L. Fan, W. Yan, D. Qiu, M. W. Fu, *Compos. B Eng.* **2024**, *281*, 111570.
- [16] D. E. Jodi, J. Park, N. Park, *Mater. Charact.* **2019**, *157*, 109888.
- [17] I. Moravcik, J. Cizek, L. de Almeida Gouvea, J. Cupera, I. Guban, I. Dlouhy, *Entropy* **2019**, *21*, 363.
- [18] D. E. Jodi, N. Choi, J. Park, N. Park, *Metall. Mater. Trans. A* **2020**, *51*, 3228.
- [19] I. Moravcik, H. Hadraba, L. Li, I. Dlouhy, D. Raabe, Z. Li, *Scr. Mater.* **2020**, *178*, 391.
- [20] I. Moravcik, N. S. Peighamardoust, A. Motallebzadeh, L. Moravcikova-Gouvea, C. Liu, J. M. Prabhakar, I. Dlouhy, Z. Li, *Mater. Charact.* **2021**, *172*, 110869.
- [21] Y. Zhang, X. H. Yan, W. B. Liao, K. Zhao, *Entropy* **2018**, *20*, 624.
- [22] J. Su, D. Raabe, Z. Li, *Acta Mater.* **2019**, *163*, 40.
- [23] I. Moravcik, V. Hornik, P. Minárik, L. Li, I. Dlouhy, M. Janovska, D. Raabe, Z. Li, *Mater. Sci. Eng. A* **2020**, *781*, 139242.
- [24] J. Wang, J. Zou, H. Yang, L. Zhang, Z. Liu, X. Dong, S. Ji, *J. Mater. Sci. Technol.* **2022**, *127*, 61.
- [25] J. Schindelin, I. Arganda-Carreras, E. Frise, V. Kaynig, M. Longair, T. Pietzsch, S. Preibisch, C. Rueden, S. Saalfeld, B. Schmid, J.-Y. Tinevez, D. J. White, V. Hartenstein, K. Eliceiri, P. Tomancak, A. Cardona, *Nat. Methods* **2012**, *9*, 676.
- [26] F. Bachmann, R. Hielscher, H. Schaeben, *Solid State Phenom.* **2010**, *160*, 63.
- [27] J. O. Andersson, T. Helander, L. Höglund, P. Shi, B. Sundman, *Calphad* **2002**, *26*, 273.
- [28] A. G. Svyazhin, J. Siwka, Z. Skuza, *Metal Sci. Heat Treat.* **2000**, *42*, 467.
- [29] A. G. Svyazhin, L. M. Kaputkina, V. E. Bazhenov, Z. Skuza, E. Siwka, V. E. Kindop, *Phys. Met. Metall.* **2015**, *116*, 552.
- [30] X. Gong, K. Chou, in *TMS 2015 144th Annu. Meet. Exhib.*, Springer, Cham **2015**, pp. 461–468.
- [31] M. R. Rolchigo, M. Y. Mendoza, P. Samimi, D. A. Brice, B. Martin, P. C. Collins, R. LeSar, *Metall. Mater. Trans.* **2017**, *48*, 3606.
- [32] X. Liu, C. Zhao, X. Zhou, Z. Shen, W. Liu, *Mater. Des.* **2019**, *168*, 107677.
- [33] A. B. Spierings, K. Dawson, P. J. Uggowitzer, K. Wegener, *Mater. Des.* **2018**, *140*, 134.
- [34] D. Walton, W. A. Tiller, J. W. Rutter, W. C. Winegard, *JOM* **1955**, *7*, 1023.
- [35] B. Chalmers, in *Applied Solid State Physics*, Springer, Boston, MA **1970**, pp. 161.
- [36] H. Fredriksson, U. Akerlind, in *Solidification and Crystallization Processing in Metals and Alloys*, Wiley, New York, NY **2012**.
- [37] Z. Sun, X. Tan, S. B. Tor, C. K. Chua, *NPG Asia Mater.* **2018**, *10*, 127.
- [38] M.-S. Pham, B. Dovgvy, P. A. Hooper, C. M. Gourlay, A. Piglione, *Nat. Commun.* **2020**, *11*, 749.
- [39] Z. Zhang, H. Sheng, Z. Wang, B. Gludovatz, Z. Zhang, E. P. George, Q. Yu, S. X. Mao, R. O. Ritchie, *Nat. Commun.* **2017**, *8*, 14390.
- [40] C. Kusuma, *Master Thesis*, Wright State University, **2016**.
- [41] D. F. Louw, P. G. H. Pistorius, *Int. J. Adv. Manuf. Technol.* **2019**, *103*, 2277.
- [42] P. Niu, R. Li, K. Gan, T. Yuan, S. Xie, C. Chen, *Metall. Mater. Trans. A* **2021**, *52*, 753.
- [43] M. Vaidya, G. M. Muralikrishna, B. S. Murty, *J. Mater. Res.* **2019**, *34*, 664.
- [44] N. Ramachandiran, H. Asgari, F. Dibia, R. Eybel, A. Keshavarzkermani, A. Gerlich, E. Toyserkani, *Mater. Sci. Eng. A* **2023**, *865*, 144633.
- [45] J. Schröder, A. Evans, E. Polatidis, J. Čapek, G. Mohr, I. Serrano-Munoz, G. Bruno, *J. Mater. Sci.* **2022**, *57*, 15036.
- [46] K. Ning, D. Bai, X. You, H. Zhang, F. Liu, *J. Phys. Conf. Ser.* **2023**, *2447*, 012004.
- [47] Y. Liu, J. Zhang, Z. Pang, *Opt. Laser Technol.* **2018**, *98*, 23.
- [48] Y. Liu, Z. Pang, J. Zhang, *Appl. Phys. A Mater. Sci. Process.* **2017**, *123*, 688.
- [49] Y. Wu, S. Zhang, X. Cheng, H. Wang, *J. Alloys Compd.* **2019**, *799*, 325.
- [50] W. Woo, J. S. Jeong, D.-K. Kim, C. M. Lee, S.-H. Choi, J.-Y. Suh, S. Y. Lee, S. Harjo, T. Kawasaki, *Sci. Rep.* **2020**, *10*, 1350.